Identification of the active sites of Cu-ZnO catalysts for water gas shift and CO hydrogenation reactions

Zhenhua Zhang
University of Science and Technology of China
Xuanye Chen
University of Science and Technology of China
Jincan Kang
Xiamen University
Zongyou Yu
University of Science and Technology of China
Jie Tian
University of Science and Technology of China
Zhongmiao Gong
Suzhou Institute of Nano-tech and Nano-bionics
Aiping Jia
Zhejiang Normal University
Rui You
University of Science and Technology of China
Kun Qian
University of Science and Technology of China
Shun He
Xiamen University
Botao Teng
Zhejiang Normal University
Yi Cui
Chinese Academy of Sciences https://orcid.org/0000-0002-9182-9038
Ye Wang
Xiamen University https://orcid.org/0000-0003-0764-2279
Wenhua Zhang
University of Science and Technology of China https://orcid.org/0000-0002-0075-385X
Weixin Huang (huangwx@ustc.edu.cn)
University of Science and Technology of China https://orcid.org/0000-0002-5025-3124

Article

Keywords: catalysts, CO hydrogenation reactions, water gas shift

Posted Date: January 13th, 2021

DOI: https://doi.org/10.21203/rs.3.rs-137209/v1

Version of Record: A version of this preprint was published at Nature Communications on July 15th, 2021. See the published version at https://doi.org/10.1038/s41467-021-24621-8.

Identification of the active sites of Cu-ZnO catalysts for water gas shift and CO hydrogenation reactions

Zhenhua Zhang[1,2#], Xuanye Chen[1,2#], Jincan Kang[3#], Zongyou Yu[1,2], Jie Tian[4], Zhongmiao Gong[5], Aiping Jia[1,2,6], Rui You[1,2], Kun Qian[1,2], Shun He[3], Botao Teng[6], Yi Cui[5], Ye Wang[3]*, Wenhua Zhang[1]*, Weixin Huang[1,2,7]*

[1] Hefei National Laboratory for Physical Sciences at the Microscale, CAS Key Laboratory of Materials for Energy Conversion, School of Chemistry and Materials Science, University of Science and Technology of China, Hefei 230026, China.

[2] Key Laboratory of Surface and Interface Chemistry and Energy Catalysis of Anhui Higher Education Institutes, University of Science and Technology of China, Hefei 230026, China.

[3] State Key Laboratory of Physical Chemistry of Solid Surfaces, Collaborative Innovation Center of Chemistry for Energy Materials, National Engineering Laboratory for Green Chemical Productions of Alcohols, Ethers and Esters, College of Chemistry and Chemical Engineering, Xiamen University, Xiamen 361005, China.

[4] Engineering and Materials Science Experiment Center, University of Science and Technology of China, Hefei 230026, China.

[5] Vacuum Interconnected Nanotech Workstation, Suzhou Institute of Nano-Tech and Nano-Bionics, Chinese Academy of Sciences, Suzhou 215123, China.

[6] Key Laboratory of the Ministry of Education for Advanced Catalysis Materials, Institute of Physical Chemistry, Zhejiang Normal University, Jinhua 321004, China.

[7] Dalian National Laboratory for Clean Energy, Dalian 116023, China.

[#] These authors contribute equally.

*To whom correspondence should be addressed: huangwx@ustc.edu.cn (WH);

whhzhang@ustc.edu.cn (WZ); wangye@xmu.edu.cn (YW).

Abstract: Cu-ZnO-Al_2O_3 catalysts are used as the industrial catalysts for water gas shift (WGS) and CO hydrogenation to methanol reactions. Herein, via a comprehensive experimental and theoretical calculation study of a series of ZnO/Cu nanocrystals inverse catalysts with well-defined Cu structures, we report that the Cu-ZnO catalysts undergo Cu structure-dependent and reaction-sensitive in situ restructuring during WGS and CO hydrogenation reactions under typical reaction conditions, forming the active sites of $Cu_{Cu(100)}$-hydroxylated ZnO ensemble and $Cu_{Cu(611)}Zn$ alloy, respectively. These results conclude the long-existing debates and provide the feasible guideline for optimizing the structures of Cu-ZnO-Al_2O_3 catalysts.

Since the postulation of the "active site" concept,[1] identifications of the active site of a catalyst have always been the Holy Grail of heterogeneous catalysis studies.[2-6] The active site of a catalyst varies with the reaction being catalyzed. Cu-ZnO-Al_2O_3 catalysts, industrially used as the catalysts for the important water gas shift (WGS) reaction ($CO + H_2O \rightarrow CO_2 + H_2$)[7] and CO hydrogenation to methanol reaction ($CO + 2H_2 \rightarrow CH_3OH$),[8] are a representative example. This has inspired great efforts devoted to identifying the active sites of Cu-ZnO-Al_2O_3 catalysts in both reactions. However, strong debates exist due to the lack of solid experimental evidence. In the Cu-ZnO based catalysts for the WGS reaction, it is argued whether the metallic copper phase with a unique structure dispersed or stabilized by ZnO[9-11] or the Cu-ZnO interface capable of facilely dissociating H_2O[12-15] acts as the active structure. Moreover, different reaction mechanisms were put forward in DFT calculations due to the lack of accurate active sites.[11-13] In the Cu-ZnO based catalysts for the CO hydrogenation to methanol reaction, the in situ formed CuZn alloy via the reduction of partial ZnO has been proposed as the active phase,[16, 17] whereas an intimate synergy between Cu and ZnO at the Cu-ZnO interface with ZnO as a structural modifier, hydrogen reservoir, or direct promoter for bond activation was highlighted in the CO_2 hydrogenation to methanol reaction with the unavoidable presence of CO.[18-20] Meanwhile, the active structures of Cu in both types of Cu-ZnO-Al_2O_3 catalysts are not established.

Uniform nanocrystals (NCs)-based catalytic materials with well-defined structures have demonstrated the successful applications in both fundamental catalysis studies under working conditions and efficient catalyst explorations.[21-25] For examples, the use of uniform cubic, octahedral and rhombic dodecahedral Cu_2O NCs that selectively expose

60 the {100}, {111} and {110} facets, respectively, enabled the identification of the active
61 sites of Cu-based catalysts in CO oxidation,[26, 27] propylene oxidation,[28] low-temperature
62 WGS reaction[29] and (photo)catalytic CO_2 hydrogenation.[30] Herein, via a combined
63 experimental and theoretical study of various ZnO/Cu-NCs inverse catalysts, we have
64 successfully identified the active sites of Cu-ZnO catalysts for WGS and CO
65 hydrogenation reactions respectively as the $Cu_{Cu(100)}$-hydroxylated ZnO ensemble and
66 $Cu_{Cu(611)}Zn$ alloy and elucidated the reaction mechanisms, which nicely exemplify the
67 concept of reaction-dependent restructuring and active site of a catalyst.

68 A series of ZnO/Cu-NCs catalysts were prepared from the corresponding
69 ZnO/Cu_2O-NCs catalysts via a morphology-preserved reduction strategy. Uniform
70 capping ligands-free Cu_2O NCs, including cubic Cu_2O NCs (c-Cu_2O) enclosed with {100}
71 crystal planes with different size distributions of 682±92 (denoted as c-Cu_2O-682),
72 109±10 (denoted as c-Cu_2O-109), and 34±4.5 (denoted as c-Cu_2O-34) nm, octahedral
73 Cu_2O NCs enclosed with {111} crystal planes with size distribution of 583±74 nm
74 (denoted as o-Cu_2O), and rhombic dodecahedral Cu_2O NCs enclosed with {110} crystal
75 planes with size distribution of 550±93 nm (denoted as d-Cu_2O) (Figure 1 A1-E1,
76 Figure S1 and Figure S2), were prepared according to well established procedures[26-29]
77 and then used as the supports to synthesize a series of ZnO/Cu_2O-NCs catalysts with
78 preserved morphologies of corresponding Cu_2O NCs supports (Figure 1 A2-E2, Table S1,
79 and Figure S3-Figure S7). The Cu_2O NCs and ZnO/Cu_2O-NCs catalysts were reduced in
80 5% CO/Ar at appropriate temperatures chose from CO-TPR results (Figure S8) to acquire
81 corresponding Cu NCs and ZnO/Cu-NCs catalysts that preserve the original
82 morphologies (Figure 1 A3-E3, A4-E4, and Figure S4-Figure S7). Only the metallic Cu

phase was observed on Cu NCs and ZnO/Cu-NCs catalysts (Figure S9), but the presence of surface Cu(I) species was identified by XPS (Figure S10).

As measured by the in-situ diffuse reflectance infrared Fourier transformed spectroscopy (DRIFTS) (Figure S11), ZnO barely adsorbs CO, while Cu_2O NCs exhibit two vibrational bands at 2108 and 2120-2145 cm^{-1} assigned to CO adsorbed respectively at the terrace and defective Cu(I) sites.[27, 31] c-Cu NCs show two vibrational bands at 2085 and 2101-2106 cm^{-1} arising from CO adsorbed respectively at the terrace and defective sites of Cu{100} facets (Figure 1F and Figure S12).[29, 32] Among all c-Cu NCs, the finest c-Cu-34 NCs exhibit the highest density of defective sites, while c-Cu-109 NCs finer than c-Cu-682 NCs exhibit a lower density of defective sites, which can be associated with different synthesis methods of various c-Cu_2O NCs and a lower reduction temperature adopted for the reduction of c-Cu_2O-109 NCs. o-Cu NCs show two vibrational bands at 2075 and 2107 cm^{-1} arising from CO adsorbed respectively at the terrace and defective sites of Cu{111} facets (Figure 1H and Figure S13).[29, 32] d-Cu NCs show one vibrational band at 2093 cm^{-1} arising from CO adsorbed at the terrace sites of Cu{110} facets (Figure 1I and Figure S13).[32] The absence of vibrational features for CO adsorbed at the Cu(I) site suggests that the surface Cu(I) species on Cu NCs is O-terminated Cu suboxide (Cu_xO, $x \geq 10$).[29] In addition to the vibrational features of CO adsorbed on the Cu surface, all ZnO/Cu-NCs catalysts exhibit a weak vibrational feature at 2130-2137 cm^{-1}, characteristic for CO adsorbed at the Cu(I) site (Figure 1 G-I, Figures S12 and S13). Its intensity initially increases but then decreases as the ZnO loading increasing, indicating that the Cu(I) site is located at the ZnO-Cu interface. These assignments are supported by density functional theory (DFT) calculation results of vibrational frequencies of CO

adsorbed on various Cu surfaces and ZnO-Cu interfaces (Figure S14). The step Cu(211) and Cu(611) surfaces were used to model the common step defects on Cu(111) and Cu(100) surfaces, respectively.[16, 33] The calculated vibrational frequency of CO adsorbed on Cu(100) is larger than on Cu(111), and those on the step sites are larger than on the corresponding terrace sites by less than 10 cm^{-1}. Resulting from the charge transfer, the copper atom of Cu-O-Zn interface is Cu(I) at which adsorbed CO exhibits a vibrational frequency higher than CO adsorbed on the terrace Cu site by more than 35 cm^{-1}.

Catalytic performances of various Cu NCs and ZnO/Cu-NCs catalysts were evaluated in the WGS and CO hydrogenation reactions. In the WGS reaction, c-Cu NCs are more active than d-Cu and o-Cu NCs (Figure S15), agreeing with the previous report.[29] Their catalytic activity increases as the sizes decrease whereas the stability decreases. ZnO/Cu NCs show much enhanced catalytic activity and stability than corresponding Cu NCs (Figure 2A and Figure S16-Figure S19), and 5%ZnO/c-Cu-109 and 9%ZnO/c-Cu-34 are even more active than the commercial $Cu/ZnO/Al_2O_3$ WGS catalyst below 423 K, despite of the large Cu particles. Calculated from the corresponding Arrhenius plots (Figure S16-Figure S18), all ZnO/c-Cu catalysts show similar apparent activation energies (E_a) of 37.7±0.3 kJ/mol and thus exhibit the same type of active site, while ZnO/d-Cu, ZnO/o-Cu, $Cu/ZnO/Al_2O_3$, c-Cu and d-Cu exhibit apparent activation energies (E_a) of 40.7±2.6, 55.9±3.9, 51.6±3.7, 54.1±3.1 and 68.4±8.0 kJ/mol, respectively (Figure 2B). Thus, the Cu{100} facets exposed on c-Cu NCs are the most active facet not only for the Cu catalysts[29] but also for the ZnO/Cu catalysts in the WGS reaction. These results suggest that the high apparent catalytic activity of commercial $Cu/ZnO/Al_2O_3$ WGS catalyst should result from the density of the active site

129 rather than from the intrinsic activity of the active site. The CO conversions of various
130 ZnO/c-Cu catalysts at 423 K, at which temperature the c-Cu catalysts do not exhibit
131 observable catalytic activity, were found proportional to the amount of CO adsorbed at
132 the Cu(I) site of Cu-O-Zn interface (Figure 2C and Figure S20). This demonstrates that
133 the low-temperature WGS reaction proceeds at the Cu-ZnO interface of ZnO/c-Cu
134 catalysts.

135 The temperature-programmed surface reaction (TPSR) spectra of CO and H_2O
136 (Figure 2D and Figure S21) demonstrate the simultaneous productions of CO_2 and H_2O
137 over ZnO/Cu-NCs catalysts, which occurs at much lower temperatures over ZnO/c-Cu
138 than over ZnO/o-Cu. This further supports that the ZnO/c-Cu catalysts are more
139 intrinsically active than the ZnO/o-Cu catalysts, and meanwhile, demonstrates that the
140 CO_2 and H_2 productions over ZnO/Cu-NCs catalysts result from the same elementary
141 surface reaction or that neither CO_2 production nor H_2 production is the rate-limiting step.
142 However, in the TPSR spectra of CO and H_2O in our previous results over Cu NCs,[29] the
143 H_2 production occurs at a higher temperature than the CO_2 production, indicating the H_2
144 production as the rate-limiting step in the Cu-catalyzed WGS reaction with the Cu-Cu_xO
145 interface as the active site.

146 Near-ambient pressure X-ray photoelectron spectroscopy (NAP-XPS) results
147 (Figure 2E, Figures S22 and S23, Table S2) show that the Cu and Zn speciation of
148 ZnO/Cu-NCs catalysts do not vary with the reaction condition, suggesting that the WGS
149 reaction catalyzed by the Cu-ZnO interface should not follow the redox mechanism.[7]
150 Hydroxyl and various surface oxygenates, including carboxylate, formate and carbonate,
151 were observed as the surface intermediates. Acquired by CO reduction, 1%ZnO/o-Cu

shows a larger OH coverage on 9%ZnO/c-Cu-34 (Figure 2F), demonstrating the lower reactivity of OH species on 1%ZnO/o-Cu toward CO. The OH species on 9%ZnO/c-Cu-34 during the WGS reaction at 323 K increases at the expense of the $O_{ZnO+CuxO}$ species, corresponding to H_2O dissociation at the c-Cu-ZnO interface to produce OH species. With the reaction temperature increasing, the OH coverage keeps decreasing while the oxygenates coverage does not vary much, suggesting that the OH species should be involved in the rate-limiting step but the oxygenates should not. The oxygenates species on 1%ZnO/o-Cu increases at the expense of OH species during the WGS reaction at 323 K, corresponding to the consumption of OH species due to the reaction with gaseous CO to produce surface oxygenates. Their coverage decreases at 423 K and the OH coverage increases, demonstrating the occurrence of surface reactions of oxygenate species and water dissociation; then the coverages of both oxygenates and OH species slightly decrease at 523 K. The coverages of OH and oxygenates surface intermediates are always larger on 1%ZnO/o-Cu catalysts under WGS reaction than on corresponding 9%ZnO/c-Cu-34 catalysts; meanwhile, the concentrations of gaseous CO and H_2O of WGS reaction catalyzed by 1%ZnO/o-Cu are higher than by 9%ZnO/c-Cu-34. These observations demonstrate that the H_2O activation are more facile and the formed OH and oxygenates intermediates are more reactive on 9%ZnO/c-Cu-34 than on 1%ZnO/o-Cu, leading to its higher activity in catalyzing the WGS reaction. This is further supported by the NAP-XPS results of 1%ZnO/o-Cu and 9%ZnO/c-Cu-34 catalysts exposed firstly to water and then to CO (Figures S24 and S25, Table S3).

DFT calculations were carried out at the ZnO/Cu(111) and ZnO/Cu(100) surfaces (Figure 3 A1 and A2) to explore the WGS reaction mechanism catalyzed by ZnO/Cu-

NCs catalysts (Figures S26 and S27, Table S4). Water dissociation into OH_{Cu} and $O_{ZnO}H$ at the ZnO-Cu interfaces proceeds very facilely, consistent with previous reports.[12, 34] The $COOH_{Cu}$ intermediate formed by adsorbed CO_{Cu} and OH_{Cu} decomposes either to produce gaseous CO_2 and $O_{ZnO}H$[35] or to produce gaseous CO_2 and H_{Cu}[29] with activation energies below 0.65 eV. However, the subsequent H_2 production either via the recombinative desorption of two $O_{ZnO}H$ groups or via the H transfer from $O_{ZnO}H$ group to the Cu site followed by the recombination of two H_{Cu} species need to overcome barriers larger than 1.39 eV. These DFT calculation results will lead to H_2 productions at a higher temperature than CO_2 productions, against our TPSR experimental results of simultaneous H_2 and CO_2 productions. Indicated by the DFT calculation results, an accumulation of OH groups can be expected at the Cu-ZnO interface. The calculated activation energy of water dissociation was found to increase with the OH coverage at the Cu-ZnO interface while the calculated activation energy of H transfer reaction to decrease (Figure 3C, Figure S28 and Table S5). The activation energy of H_2O dissociation increases to 1.05 and 0.87 eV respectively at the 0.75 ML OH_{ZnO}-ZnO-Cu(111) (Figure 3B1) and 0.75 ML OH_{ZnO}-ZnO-Cu(100) (Figure 3B2) interfaces, while the activation energy of subsequent H transfer reaction decreases to 0.88 and 0.76 eV, respectively, leading to H_2O dissociation as the rate-limiting step of WGS reaction. Meanwhile, all elementary steps proceed more easily at the 0.75 ML OH_{ZnO}-ZnO-Cu(100) interface than at the 0.75 ML OH_{ZnO}-ZnO-Cu(111) interface (Figure 3D, Figure S29 and Table S6). The calculation results on 0.75 ML OH_{ZnO}-ZnO/Cu surfaces agree well with the above experimental observations. Thus, the Cu-hydroxylated ZnO ensemble is the active site of Cu/ZnO catalysts to catalyze the WGS reaction, and the $Cu_{Cu(100)}$-

198 hydroxylated ZnO ensemble is more active than the $Cu_{Cu(111)}$-hydroxylated ZnO
199 ensemble.

200 In the steady-state CO hydrogenation reaction at 523 K (Figure 4A and Table S7), o-
201 Cu and c-Cu NCs dominantly yield CH_4, agreeing with previous results of unsupported
202 Cu catalysts for CO hydrogenation reaction,[36] while d-Cu NCs are inactive. The CO
203 conversion increases as the size of c-Cu NCs decreases. ZnO/d-Cu catalysts are also
204 inactive and ZnO/o-Cu catalysts exhibit similar selectivity to o-Cu NCs, while ZnO/c-Cu
205 catalysts show volcano-shaped dependent CH_3OH selectivity on the ZnO loading. The
206 highest CH_3OH selectivity among ZnO/c-Cu-682, ZnO/c-Cu-109 and ZnO/c-Cu-34 are
207 23.4% for 1%ZnO/c-Cu-682, 19.8% for 5%ZnO/c-Cu-109 and 65.9% for 9%ZnO/c-Cu-
208 34, respectively.

209 The Cu phase in all used Cu NCs and ZnO/Cu-NCs catalysts is metallic (Figure
210 S30), but used d-Cu NCs and ZnO/d-Cu catalysts were observed to be fully covered with
211 amorphous carbon thin film (Figure S31), demonstrating the occurrence of serious coking
212 that results in the catalytic inactivity. In addition to originally-existing metallic Cu and
213 ZnO components, CuZn alloy was identified on used ZnO/o-Cu and ZnO/c-Cu catalysts
214 (Figure 4B, Figure S32-Figure S35). The percentage of CuZn alloy in Zn-contained
215 components of selected used ZnO/Cu-NCs catalysts was acquired by counting more than
216 100 particles in the HRTEM images (Figure 4C) and found to correlate well to the
217 CH_3OH selectivity for the ZnO/Cu-NCs catalysts with the same type of Cu NCs support,
218 for example, ZnO/c-Cu-34. This demonstrates the in situ formation of active CuZn alloys
219 in ZnO/Cu catalysts to catalyze CO hydrogenation to CH_3OH, consistent with previous
220 reports.[16]

The CuZn alloy formation depends on the ZnO loading of ZnO/Cu-NCs catalysts. H_2-TPR profiles of various ZnO/Cu-NCs catalysts (Figures S36 and S37) show that the appearance of reduction peak for supported large ZnO particles corresponds to the decrease in the percentage of CuZn alloy. This suggests that highly-dispersed ZnO is more facile to alloy with Cu substrates than ZnO aggregates during CO hydrogenation reaction, agreeing with previous results.[17] The CuZn alloy formation also depends on the structure of Cu NCs supports. Not all highly-dispersive ZnO species can form the CuZn alloy. With similar ZnO loadings and Cu NCs sizes, the percentage of CuZn alloy in used 1%ZnO/c-Cu-682 catalyst is much higher than in used 1%ZnO/o-Cu catalyst, suggesting more facile formation of CuZn alloy on c-Cu NCs than on o-Cu NCs. The percentage of CuZn alloy in different series of used ZnO/c-Cu catalysts does not follow an order of the surface areas of c-Cu NCs, but follows the same order of ZnO/c-Cu-34 > ZnO/c-Cu-682 > ZnO/c-Cu-109 to that of the step site density on various c-Cu NCs (Figure 1F). These observations indicate that the step sites on c-Cu surfaces are the dominant site for the CuZn alloy formation during CO hydrogenation reaction. The CuZn alloy was previously observed to preferentially form at the step sites of Cu particles in industrial $Cu/ZnO/Al_2O_3$ catalyst for CO hydrogenation to CH_3OH.[16]

In the in situ DRIFTS during CO hydrogenation reaction (Figure 4D, Figure S38-Figure S41 and Table S8), 9%ZnO/c-Cu-34 with a high CH_3OH selectivity exhibits strong vibrational features of adsorbed CH_3O_a and CH_3OH_a, suggesting the CH_3O_a hydrogenation as the rate-limiting step of CO hydrogenation to CH_3OH,[16, 37] while c-Cu-34 with a high CH_4 selectivity exhibits significantly-weakened vibrational features of adsorbed CH_3O_a and CH_3OH_a but vibrational features of adsorbed CH_2OH_a, $CH_{2,a}$, $CH_{3,a}$

and gaseous CH_4, supporting that CO hydrogenation to CH_4 proceeds via the CH_2OH_a intermediate reacting with adsorbed H_a to form $CH_{2,a}$.[38] An in situ reactor for transmission FT-IR measurements under conditions varying from high pressures and high temperatures to vacuum and low temperatures was used to firstly characterize various catalysts under CO hydrogenation reaction and then probe their structures by CO adsorption at low temperature. The acquired in situ transmission FT-IR spectra under CO hydrogenation reaction are similar to the corresponding in situ DRIFTS spectra (Figure S42). During the subsequent CO adsorption (Figure 4E and Figure S43), a vibrational feature at 2075 cm^{-1} arising from Cu{111} facets appears on all used Cu NCs and ZnO/Cu-NC catalysts except on used d-Cu NCs which exhibits no feature due to the entire capsulation by carbon thin film; meanwhile, an additional vibrational band appears at ~2060 cm^{-1} for used ZnO/Cu-NC, which, based on previous[39] and our DFT calculations of CO adsorbed on Zn-Cu(611) and Zn-Cu(211) alloy surfaces (Figure S44), can be assigned to CO adsorbed on CuZn alloy. These observations suggest that only the Cu{111} facets on bare Cu surfaces of used catalysts act to catalyze CO hydrogenation to CH_4 under the employed condition while other originally-existing Cu facets and defective sites with low-coordinated Cu atoms on bare Cu surfaces are poisoned by coke formation. The CH_3OH formation rates over various ZnO/c-Cu catalysts were found proportional to the amount of CO adsorbed on CuZn alloy of corresponding used catalysts (Figure 4F, Figure S45); meanwhile, the CH_3OH formation rate is much smaller over 1% ZnO/o-Cu catalyst than over ZnO/c-Cu catalysts with similar amounts of CO adsorbed on CuZn alloy. This directly demonstrates that CuZn alloy is the active component of ZnO/Cu-NC

266 catalysts to catalyze CO hydrogenation to CH_3OH and more active CuZn alloy form on
267 ZnO/c-Cu catalysts than on ZnO/o-Cu catalysts.

268 The activation energy for CuZn alloy formation of ZnO on various Cu surfaces was
269 calculated to follow an order of ZnO/Cu(611) < ZnO/Cu(211) < ZnO/Cu(100) <
270 ZnO/Cu(111) (Figure 5A and Figure S46), agreeing with the experimental results that the
271 step sites on Cu NCs are the dominant site for CuZn alloy formation and the CuZn alloy
272 formation is more facile on the step sites of c-Cu NCs than of o-Cu NCs. Meanwhile, the
273 calculated reaction mechanism of CO hydrogenation to CH_3OH (Figure 5B, Figure S47,
274 and Table S9) demonstrates that adsorbed CH_3O_a hydrogenation is the rate-limiting step
275 and proceeds with a smaller activation energy on Zn-Cu(611) alloy surface than on Zn-
276 Cu(211) alloy surface, consistent with the experimental observations of CH_3O_a and
277 CH_3OH_a as the surface intermediates and of a higher catalytic activity of CuZn alloy
278 formed on ZnO/c-Cu than on ZnO/o-Cu. Thus, $Cu_{Cu(611)}Zn$ alloy is the active site of Cu-
279 ZnO catalysts for catalyzing CO hydrogenation reaction to CH_3OH.

280 Thus, the ZnO/Cu catalysts undergo different in situ restructuring processes during
281 WGS and CO hydrogenation reactions under typical reaction conditions to form the Cu-
282 hydroxylated ZnO ensemble and CuZn alloy active sites, respectively. These results
283 demonstrate reaction-sensitive restructuring and active sites of Cu-ZnO catalysts.
284 Moreover, the in situ restructuring processes are modulated by the Cu structure to form
285 the active sites with highest intrinsic catalytic activity, $Cu_{Cu(100)}$-hydroxylated ZnO
286 ensemble and $Cu_{Cu(611)}Zn$ alloy for WGS and CO hydrogenation reactions, respectively.
287 Considering the identified active sites, fabricating Cu-ZnO catalysts with Cu{100} facets
288 as many as possible and with Cu{611} step sites as many as possible are effective

289 strategies to develop highly efficient Cu-ZnO catalysts for water gas shift and CO
290 hydrogenation reactions, respectively.

Methods

All chemicals were purchased from Sinopharm Chemical Reagent Co., Ltd. and used without further purification. 5% CO/Ar, 5% H_2/Ar, 66.7% H_2/33.3% CO, 0.432% CO/Ar, O_2 (99.999%), Ar (99.999%), C_3H_6 (99.95%), N_2 (99.999%), and CO (99.99%) were purchased from Nanjing Shangyuan Industrial Factory and used without further purification. Ultrapure water (>18.5 MΩ) was used.

Cu_2O cubes with size distribution of 682±92 nm and octahedra with size distribution of 583±74 nm were synthesized according to Zhang *et al.*'s method.[40] Typically, 5 mL of NaOH aqueous solution (2.0 mol·L^{-1}) was added dropwise into 50 mL of $CuCl_2$ aqueous solution (0.01 mol·L^{-1}) at 328 K under continuous stirring (Cu_2O octahedra containing 4.44 g of poly(vinylpyrrolidone) (PVP)). After stirring for 0.5 h, 5 mL of ascorbic acid (AC) solution (0.6 mol·L^{-1}) was subsequently added dropwise into the solution. The mixture was stirred at 328 K for additional 5 h. The acquired precipitate was collected by centrifugation, decanted by repeated washing with ultrapure water and absolute ethanol for several times, and finally dried in vacuum at room temperature for 12 h. The acquired cubic and octahedral Cu_2O nanocrystals (NCs) were denoted as c-Cu_2O-682 and o-Cu_2O-PVP, respectively.

Cu_2O cubes with size distributions of 109±10 and 34±4.5 nm were synthesized according to Chang *et al.*'s method.[41] Typically, 1 mL of $CuSO_4$ aqueous solution (1.2 mol·L^{-1}) was rapidly added into 400 mL ultrapure water at 298 K (Cu_2O cubes with size distribution of 109±10 nm containing 0.26 g of sodium citrate). After stirring for 5 min, 1 mL of NaOH aqueous solution (4.8 mol·L^{-1}) was added into the solution. The solution color turned from clear blue solution immediately to turbid blue, indicating $Cu(OH)_2$

314 formed. After stirring for another 5 min, 1 mL of AC aqueous solution (1.2 mol·L^{-1}) was
315 added as a reducer and the resulting solution was maintained for additional 0.5 h at 298 K.
316 The solution color gradually turned from turbid blue to yellowish brown. The acquired
317 precipitate was collected by centrifugation, decanted by repeated washing with ultrapure
318 water and absolute ethanol for several times, and finally dried in vacuum at room
319 temperature for 12 h. The acquired Cu_2O NCs with size distributions of 109±10 and
320 34±4.5 nm were denoted as c-Cu_2O-109 and c-Cu_2O-34, respectively.

321 Cu_2O rhombic dodecahedra with size distribution of 550±93 nm were synthesized
322 according to Liang *et al.*'s method.[42] Typically, 4 mL of oleic acid (OA) mixed with 20
323 mL of absolute ethanol was added into 40 mL of $CuSO_4$ aqueous solution (0.025 mol·L^{-1})
324 under continuous stirring at 373 K. Then, 10 mL of NaOH aqueous solution (0.8 mol·L^{-1})
325 was added. After stirring for 5 min, 30 mL of D-(+)-glucose aqueous solution (0.63
326 mol·L^{-1}) was added. The resulting mixture were further stirred at 373 K for 1 h to acquire
327 a brick-red precipitate. Centrifugation, decantation by repeating washing with ultrapure
328 water and absolute ethanol for several times were performed, and the final precipitate was
329 dried in vacuum at room temperature for 12 h. The acquired rhombic dodecahedral Cu_2O
330 NCs were denoted as d-Cu_2O-OA.

331 The remove of capping ligands (PVP on o-Cu_2O-PVP and OA on d-Cu_2O-OA)
332 followed a controlled oxidation procedure developed by Hua *et al.*.[28] Typically, as-
333 synthesized Cu_2O NCs (ca. 0.2 g) were placed in a U-shaped quartz microreactor. The
334 atmosphere was first purged by the stream of C_3H_6 + O_2 + N_2 mixture (C_3H_6:O_2:N_2 =
335 2:1:22, total flow rate: 50 mL·min^{-1}) at room temperature for 30 min. Then, the sample
336 was heated to the desirable temperature at a rate of 5 K·min^{-1} (o-Cu_2O-PVP: 473 K; d-

337 Cu_2O-OA: 488 K) and kept for 30 min. Next, the steam was switched to high-pure Ar
338 (flow rate: 30 $mL \cdot min^{-1}$) in which the sample was naturally cooled to room temperature.
339 The acquired Cu_2O octahedra and rhombic dodecahedra without capping ligands were
340 denoted as o-Cu_2O and d-Cu_2O, respectively.

341 ZnO supported on Cu_2O NCs (ZnO/Cu_2O) catalysts were synthesized via incipient
342 wetness impregnation method. Typically, 200 mg of as-synthesized Cu_2O NCs were
343 adequately incipient wetness impregnated with calculated amounts of zinc nitrate
344 ($Zn(NO_3)_2 \cdot 6H_2O$) aqueous-ethanol mixture solution. The resulting sample was dried in
345 vacuum at room temperature for 12 h and then heated at 623 K in high-pure Ar with a
346 flow rate of 50 $mL \cdot min^{-1}$ for 2 h to prepare ZnO/Cu_2O catalysts. The acquired ZnO/Cu_2O
347 catalysts were further reduced in 5% CO/Ar with a flow rate of 30 $mL \cdot min^{-1}$ at
348 appropriate temperatures chose from CO-TPR results for 2 h to prepare corresponding
349 ZnO/Cu catalysts. The reduction temperatures are 548 K for c-Cu_2O-682, ZnO/c-Cu_2O-
350 682, o-Cu_2O, ZnO/o-Cu_2O, d-Cu_2O, and ZnO/d-Cu_2O, and 473 K for c-Cu_2O-109, c-
351 Cu_2O-109, ZnO/c-Cu_2O-34 and ZnO/c-Cu_2O-34.

352 Details on structural characterizations, activity evaluations, and DFT calculations
353 can be found in the supplementary information.

354

Acknowledgements

This work was financially supported by the National Key R & D Program of MOST (2017YFB0602205), the National Natural Science Foundation of China (91945301, 21525313, 91745202), the Chinese Academy of Sciences and the Changjiang Scholars Program of Ministry of Education of China. We thank Xianquan Industrial and Trading Co., Ltd. (Tianjin, China) for assistance on in situ transmission FT-IR measurements under conditions varying from high pressures and high temperatures to vacuum and low temperatures.

Author contributions. W.H. designed and supervised the project. W.Z. supervised the DFT calculations. Y.W. supervised the catalytic activity evaluation in CO hydrogenation. Z.Z. carried the catalyst preparation and characterization, and catalytic activity evaluation in WGS reaction. X.C. carried out the DFT calculations. J.K carried out the catalytic activity evaluation in CO hydrogenation. Z.Y., J.T., Z.G., A.J., R.Y., K.Q., S.H., B.T. and Y.C. assisted with the experiments. All authors analyzed the data. W.H., Z.Z. and X.C. prepared the manuscript and other authors commented on the manuscript.

Additional information.

Supplementary information is available in the online version of the paper. Reprints and permission information is available online at http://www.nature.com/reprints. Correspondence and requests for materials should be addressed to W. H.

Competing financial interests. The authors declare no competing financial interests.

References and Notes

1. Taylor, H. S. A theory of the catalytic surface. *Proc. R. Soc. Lond. A* **108**, 105-111 (1925).

2. Somorjai, G. A. Surface reconstruction and catalysis. *Annu. Rev. Phys. Chem.* 45, 721-751 (1994).

3. Hansen, P. L. *et al.* Atom-resolved imaging of dynamic shape changes in supported copper nanocrystals. *Science* **295**, 2053-2055 (2002).

4. Bell, A. T. The impact of nanoscience on heterogeneous catalysis. *Science* **299**, 1688-1691 (2003).

5. Vestergaard, E. K. *et al.* Adsorbate-induced alloy phase separation: a direct view by high-pressure scanning tunneling microscopy. *Phys. Rev. Lett.* **95**, 126101 (2005).

6. Tao, F. *et al.* Reaction-driven restructuring of Rh-Pd and Pt-Pd core-shell nanoparticles. *Science* **322**, 932-934 (2008).

7. Ratnasamy, C., Wagner, J. P. Water gas shift catalysis. *Catal. Rev.* **51**, 325-440 (2009).

8. Waugh, K. C. Methanol synthesis. *Catal. Today* **15**, 51-75 (1992).

9. Ginés, M. J. L., Amadeo, N., Laborde, M., Apesteguía, C. R. Activity of structure-sensitivity of the water-gas shift reaction over Cu-Zn-Al mixed oxide catalysts. *Appl. Catal. A.***131**, 283-296 (1995).

10. Lima, A. A. G., Nele, M., Moreno, E. L., Andrade, H. M. C. Composition effects on the activity of Cu-ZnO-Al_2O_3 based catalysts for the water gas shift reaction: a statistical approach. *Appl. Catal. A.***171**, 31-43 (1998).

11. Liu, P. Water-gas shift reaction on oxide/Cu(111): rational catalyst screening from density functional theory. *J. Chem. Phys.* **133**, 204705 (2010).

12. Studt, F., Behrens, M., Abild-Pedersen, F. Energetics of the water-gas-shift reaction on the active sites of the industrially used Cu/ZnO/Al_2O_3 catalyst. *Catal. Lett.* **144**, 1973-1977 (2014).

13. Cong, V. T., Huynh, L. K., Jiang, J.-C., Nhung, N. T. A., Tat, P. V. Density function theory study of water gas shift reaction on 2Cu/ZnO (10-10) surface, *Comput. Theor. Chem.* **1081**, 62-70 (2016).

14. Rodriguez, J. A., Liu, P., Hrbek, J., Evans, J., Pérez, M. Water gas shift reaction on Cu and Au nanoparticles supported on CeO_2(111) and ZnO(000-1): intrinsic activity and importance of support interactions. *Angew. Chem. Int. Ed.* **46**, 1329-1332 (2007).

15. Bu, Y., Weststrate, C. J., Niemantsverdriet, J. W., Fredriksson, H. O. A. Role of ZnO and CeO_x in Cu-based model catalysts in activation of H_2O and CO_2 dynamics studied by in situ ultraviolet-visible and X-ray photoelectron spectroscopy. *ACS Catal.* **6**, 7994-8003 (2016).

16. Behrens, M. *et al.* The active site of methanol synthesis over Cu/ZnO/Al_2O_3 industrial catalysts. *Science* **336**, 893-897 (2012).

17. Kuld, S. *et al.* Quantifying the promotion of Cu catalysts by ZnO for methanol synthesis. *Science* **352**, 969-974 (2016).

18. Kattel, S., Ramírez, P. J., Chen, J. G., Rodriguez, J. A., Liu, P. Active sites for CO_2 hydrogenation to methanol on Cu/ZnO catalysts. *Science* **355**, 1296-1299 (2017).

19. Choi, Y.; Futagami, K.; Fujitani, T.; Nakamura, J. The difference in the active sites for CO_2 and CO hydrogenations on Cu/ZnO-based methanol synthesis catalysts. *Catal. Lett.* **73**, 27-31 (2001).

20. Laudenschleger, D.; Ruland, H.; Muhler, M. Identifying the nature of the active sites in methanol synthesis over $Cu/ZnO/Al_2O_3$ catalysts. *Nat. Commun.* **11**, 3898 (2011).

21. Somorjai, G. A., Frei, H., Park, J. Y. Advancing the frontiers in nanocatalysis, biointerfaces, and renewable energy conversion by innovations of surface techniques. *J. Am. Chem. Soc.* **131**, 16589-16605 (2009).

22. Zhou, K., Li, Y. Catalysis based on nanocrystals with well-defined facets. *Angew. Chem. Int. Ed.* **51**, 602-613 (2012).

23. Zaera, F. Shape-controlled nanostructures in heterogeneous catalysis. *ChemSusChem* **6**, 1797-1820 (2013).

24. Huang, W. Oxide nanocrystal model catalysts. *Acc. Chem. Res.* **49**, 520-527 (2016).

25. Chen, S., Xiong, F., Huang, W. Surface chemistry and catalysis of oxide model catalysts from single crystals to nanocrystals. *Surf. Sci. Rep.* **74**, 100471 (2019).

26. Bao, H. *et al.* Crystal-plane-controlled surface restructuring and catalytic performance of oxide nanocrystals. *Angew. Chem. Int. Ed.* **50**, 12294-12298 (2011).

27. Zhang, Z. *et al.* Site-resolved Cu_2O catalysis in the oxidation of CO. *Angew. Chem. Int. Ed.* **58**, 4276-4280 (2019).

28. Hua, Q. *et al.* Crystal-plane-controlled selectivity of Cu_2O catalysts in propylene oxidation with molecular oxygen. *Angew. Chem. Int. Ed.* **126**, 4956-4961 (2014).

29. Zhang, Z. *et al.* The most active Cu facet for low-temperature water gas shift reaction. *Nat. Commun.* **8**, 488 (2017).

30. Wan, L. *et al.* Cu_2O nanocubes with mixed oxidation-state facets for (photo)catalytic hydrogenation of carbon dioxide. *Nat. Catal.* **2**, 889-898 (2019).

31. Chen, S. *et al.* Probing surface structures of CeO_2, TiO_2, and Cu_2O nanocrystals with CO and CO_2 chemisorption. *J. Phys. Chem. C* **120**, 21472-21485 (2016).

32. Dulaurent, O., Courtois, X., Perrichon, V., Bianchi, D. Heats of adsorption of CO on a Cu/Al_2O_3 catalyst using FTIR spectroscopy at high temperatures and under adsorption equilibrium conditions. *J. Phys. Chem. B* **104**, 6001-6011 (2000).

33. Hagman, B. *et al.* Steps control the dissociation of CO_2 on Cu(100). *J. Am. Chem. Soc.* **140**, 12974-12979 (2018).

34. Yang, L., Karim, A., Muckerman, J. T. Density functional kinetic monte carlo simulation of water-gas shift reaction on Cu/ZnO. *J. Phys. Chem. C* **117**, 3414-3425 (2013).

35. Mudiyanselage, K. *et al.* Importance of the metal-oxide interface in catalysis: in situ studies of the water-gas shift reaction by ambient-pressure X-ray photoelectron spectroscopy. *Angew. Chem. Int. Ed.* **52**, 5101-5105 (2013).

36. Kim, J.-Y., Lee, J. Mechanism and cross sections for HD and $CH_{4-x}D_x$ (x=1-4) formation in D(g) + CH_3/Cu(111) reaction at 100 K. *J. Chem. Phys.* **112**, 6015-6022 (2000).

37. Martínez-Suárez, L., Siemer, N., Frenzel, J., Marx, D. Reaction network of methanol synthesis over Cu/ZnO nanocatalysts. *ACS Catal.* **5**, 4201-4218 (2015).

38. Grabow, L. C., Mavrikakis, M. Mechanism of methanol synthesis on Cu through CO_2 and CO hydrogenation. *ACS Catal.* **1**, 365-384 (2011).

39. Greeley, J. *et al.* CO vibrational frequencies on methanol synthesis catalysts: a DFT study. *J. Catal.* **213**, 63-72 (2003).

40. Zhang, D. -F. *et al.* Delicate control of crystallographic facet-oriented Cu_2O nanocrystals and the correlated adsorption ability. *J. Mater. Chem.* **19**, 5220-5225 (2009).

41. Chang, I. -C. *et al.* Large-scale synthesis of uniform Cu_2O nanocubes with tunable sizes by in-situ nucleation. *CrystEngComm*, **15**, 2363-2366 (2013).

42. Liang, X., Gao, L., Yang, S., Sun, J. Facile synthesis and shape evolution of single-crystal cuprous oxide. *Adv. Mater.* **21**, 2068-2071 (2009).

Figure captions

Figure 1. Structural characterizations. TEM images of as-synthesized (**A1**) c-Cu_2O-682, (**B1**) c-Cu_2O-109, (**C1**) c-Cu_2O-34, (**D1**) o-Cu_2O, and (**E1**) d-Cu_2O NCs; TEM images of as-synthesized (**A2**) 1%ZnO/c-Cu_2O-682, (**B2**) 1%ZnO/c-Cu_2O-109, (**C2**) 1%ZnO/c-Cu_2O-34, (**D2**) 1%ZnO/o-Cu_2O, and (**E2**) 1%ZnO/d-Cu_2O catalysts; TEM and HRTEM images of as-synthesized (**A2**) 1%ZnO/c-Cu-682, (**B2**) 1%ZnO/c-Cu-109, (**C2**) 1%ZnO/c-Cu-34, (**D2**) 1%ZnO/o-Cu, and (**E2**) 1%ZnO/d-Cu catalysts; In situ DRIFTS with peak-fitting results of CO adsorption at 123 K on (F) various c-Cu NCs, (G) various 1%ZnO/c-Cu catalysts, (H) o-Cu NCs and 1%ZnO/o-Cu catalyst, and (I) d-Cu NCs and 1%ZnO/d-Cu catalyst. Lattice fringes of 1.80, 2.08, 2.50/2.51, 2.61, and 2.81 Å respectively correspond to the spacing of Cu{200}, Cu{111} (JCPDS card NO. 89-2838), hexagonal ZnO{101}, ZnO{002}, and ZnO{100} (JCPDS card NO 89-1397) crystal planes.

Figure 2. Activity evaluations and mechanism investigations in WGS reaction. (**A**) Catalytic performance of representative ZnO/Cu and commercial Cu/ZnO/Al_2O_3 WGS catalysts for the WGS reaction; (**B**) Apparent activation energies (E_a) of various Cu-based catalysts as a function of ZnO loadings; (**C**) Temperature-programmed reaction spectra of WGS reaction over 9%ZnO/c-Cu-34 and 1%ZnO/o-Cu catalysts; (**D**) CO conversion at 423 K as a function of the intensity of CO adsorbed on $Cu(I)_{Cu(100)}$-ZnO interface derived from corresponding DRIFTS results; (**E**) NAP-XPS spectra with peak-fitting results of 9%ZnO/c-Cu-34 and 1%ZnO/o-Cu catalysts under 0.33 mbar CO + 0.66 mbar H_2O at 423 K; (**F**) Variations of the intensity of oxygen-containing species on

9%ZnO/c-Cu-34 and 1%ZnO/o-Cu catalysts under 0.33 mbar CO + 0.66 mbar H_2O at different temperatures derived from corresponding NAP-XPS results.

Figure 3. DFT calculations in WGS reaction. Optimized surface structures of (**A1**) ZnO/Cu(111), (**A2**) ZnO/Cu(100), (**B1**) 0.75 ML-OH_{ZnO}-ZnO/Cu(111) and (**B2**) 0.75 ML OH_{ZnO}-ZnO/Cu(100). The reddish-orange, purple, red, and white spheres represent Cu, Zn, O, and H atoms, respectively.; (**C**) Calculated activation energy of H_2O dissociation and OH_{ZnO}-to-H_{Cu} H transfer reaction at ZnO-Cu interface as a function of the OH coverage on interfacial ZnO of ZnO/Cu(111) and ZnO/Cu(100) surfaces; (**D**) Calculated energy profiles of WGS reaction catalyzed by 0.75 ML OH_{ZnO}-ZnO/Cu(111) and 0.75 ML OH_{ZnO}-ZnO/Cu(100) surfaces.

Figure 4. **Activity evaluations and mechanism investigations in CO hydrogenation reaction. (A1-A4)** Catalytic performance of various Cu and ZnO/Cu catalysts in the CO hydrogenation to methanol reaction; Representative HRTEM images of used (**B1**) 1%ZnO/c-Cu-682 and (**B2**) 1%ZnO/o-Cu; Lattice fringes of 1.82, 2.08, and 2.13 Å respectively correspond to the spacing of Cu{100}. Cu{111} (JCPDS card NO. 89-2838), and Zn-Cu alloy {111} (JCPDS card NO 89-1397) crystal planes; (**C**) Statistical percentage of CuZn alloy nanoparticles of various ZnO/Cu catalysts derived from corresponding HRTEM images; (**D**) In situ DRIFTS spectra of c-Cu-34 and 9%ZnO/c-Cu-34 catalysts under 2 MPa 33.3% CO + 66.7% H_2 at 523 K; (**E**) In situ FT-IR spectra with peak-fitting results of CO adsorbed on various ZnO/Cu catalysts evaluated after CO hydrogenation to methanol reaction and (**F**) CH_3OH productions over various ZnO/Cu catalysts as a function of the intensity of CO adsorbed on $Cu_{defective\ Cu(100)}$-Zn alloy derived from corresponding DRIFTS results.

519 **Figure 5. DFT calculations in CO hydrogenation reaction. (A)** Calculated activation
520 energy for CuZn alloy formation of ZnO on various Cu surfaces and **(B)** Calculated
521 energy profiles of CO hydrogenation into methanol by ZnCu(211) and ZnCu(611) alloys.
522 Insets show the optimized surface structures of ZnCu(211) and ZnCu(611) alloys. The
523 reddish-orange and purple spheres represent Cu and Zn atoms, respectively.

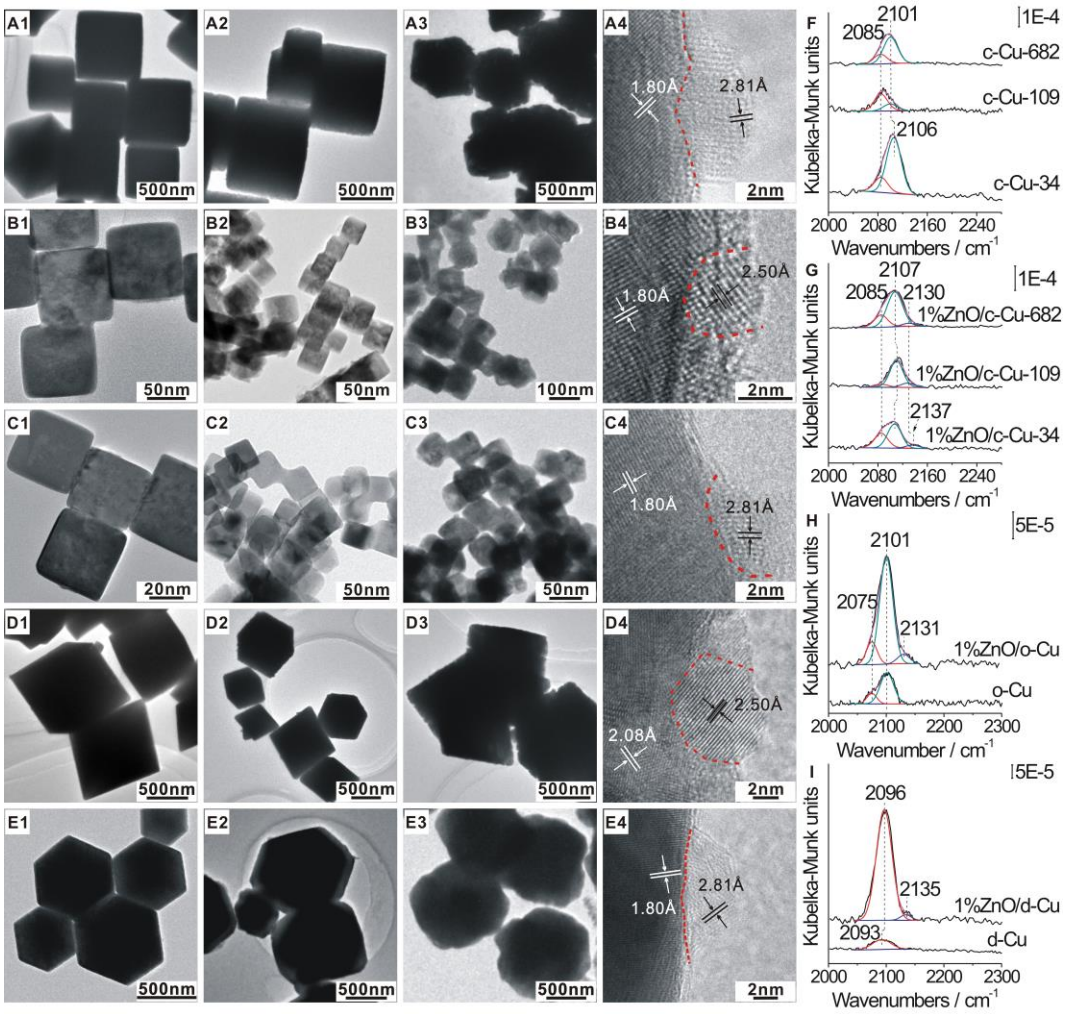

524 **Figure 1. Structural characterizations**. TEM images of as-synthesized (**A1**) c-Cu_2O-
525 682, (**B1**) c-Cu_2O-109, (**C1**) c-Cu_2O-34, (**D1**) o-Cu_2O, and (**E1**) d-Cu_2O NCs; TEM
526 images of as-synthesized (**A2**) 1%ZnO/c-Cu_2O-682, (**B2**) 1%ZnO/c-Cu_2O-109, (**C2**)
527 1%ZnO/c-Cu_2O-34, (**D2**) 1%ZnO/o-Cu_2O, and (**E2**) 1%ZnO/d-Cu_2O catalysts; TEM and
528 HRTEM images of as-synthesized (**A2**) 1%ZnO/c-Cu-682, (**B2**) 1%ZnO/c-Cu-109, (**C2**)
529 1%ZnO/c-Cu-34, (**D2**) 1%ZnO/o-Cu, and (**E2**) 1%ZnO/d-Cu catalysts; In situ DRIFTS
530 with peak-fitting results of CO adsorption at 123 K on (F) various c-Cu NCs, (G) various
531 1%ZnO/c-Cu catalysts, (H) o-Cu NCs and 1%ZnO/o-Cu catalyst, and (I) d-Cu NCs and
532 1%ZnO/d-Cu catalyst. Lattice fringes of 1.80, 2.08, 2.50/2.51, 2.61, and 2.81 Å

533 respectively correspond to the spacing of Cu{200}, Cu{111} (JCPDS card NO. 89-2838),
534 hexagonal ZnO{101}, ZnO{002}, and ZnO{100} (JCPDS card NO 89-1397) crystal
535 planes.
536

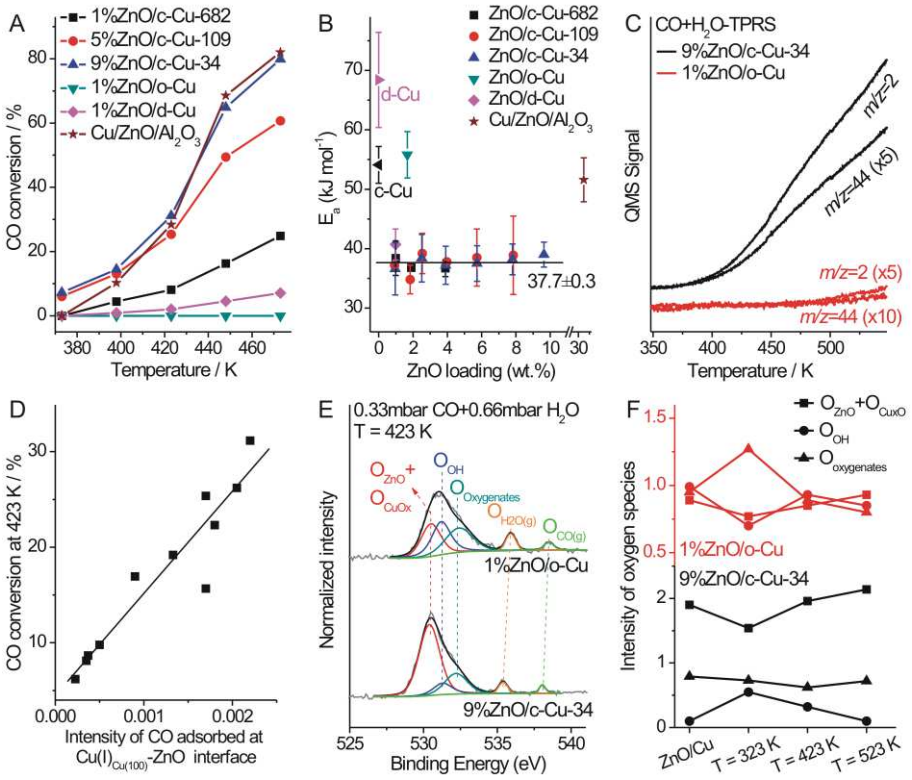

537

538 **Figure 2. Activity evaluations and mechanism investigations in WGS reaction**. (**A**)
539 Catalytic performance of representative ZnO/Cu and commercial $Cu/ZnO/Al_2O_3$ WGS
540 catalysts for the WGS reaction; (**B**) Apparent activation energies (E_a) of various Cu-
541 based catalysts as a function of ZnO loadings; (**C**) Temperature-programmed reaction
542 spectra of WGS reaction over 9%ZnO/c-Cu-34 and 1%ZnO/o-Cu catalysts; (**D**) CO
543 conversion at 423 K as a function of the intensity of CO adsorbed on $Cu(I)_{Cu(100)}$-ZnO
544 interface derived from corresponding DRIFTS results; (**E**) NAP-XPS spectra with peak-
545 fitting results of 9%ZnO/c-Cu-34 and 1%ZnO/o-Cu catalysts under 0.33 mbar CO + 0.66
546 mbar H_2O at 423 K; (**F**) Variations of the intensity of oxygen-containing species on
547 9%ZnO/c-Cu-34 and 1%ZnO/o-Cu catalysts under 0.33 mbar CO + 0.66 mbar H_2O at
548 different temperatures derived from corresponding NAP-XPS results.

549

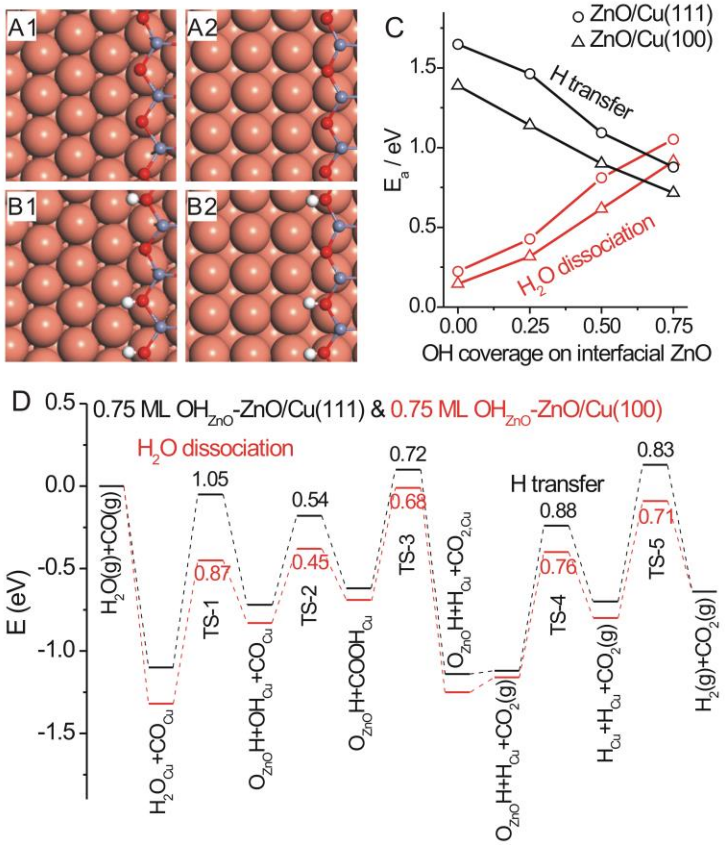

Figure 3. DFT calculations in WGS reaction. Optimized surface structures of (**A1**) ZnO/Cu(111), (**A2**) ZnO/Cu(100), (**B1**) 0.75 ML-OH_{ZnO}-ZnO/Cu(111) and (**B2**) 0.75 ML OH_{ZnO}-ZnO/Cu(100). The reddish-orange, purple, red, and white spheres represent Cu, Zn, O, and H atoms, respectively.; (**C**) Calculated activation energy of H_2O dissociation and OH_{ZnO}-to-H_{Cu} H transfer reaction at ZnO-Cu interface as a function of the OH coverage on interfacial ZnO of ZnO/Cu(111) and ZnO/Cu(100) surfaces; (**D**) Calculated energy profiles of WGS reaction catalyzed by 0.75 ML OH_{ZnO}-ZnO/Cu(111) and 0.75 ML OH_{ZnO}-ZnO/Cu(100) surfaces.

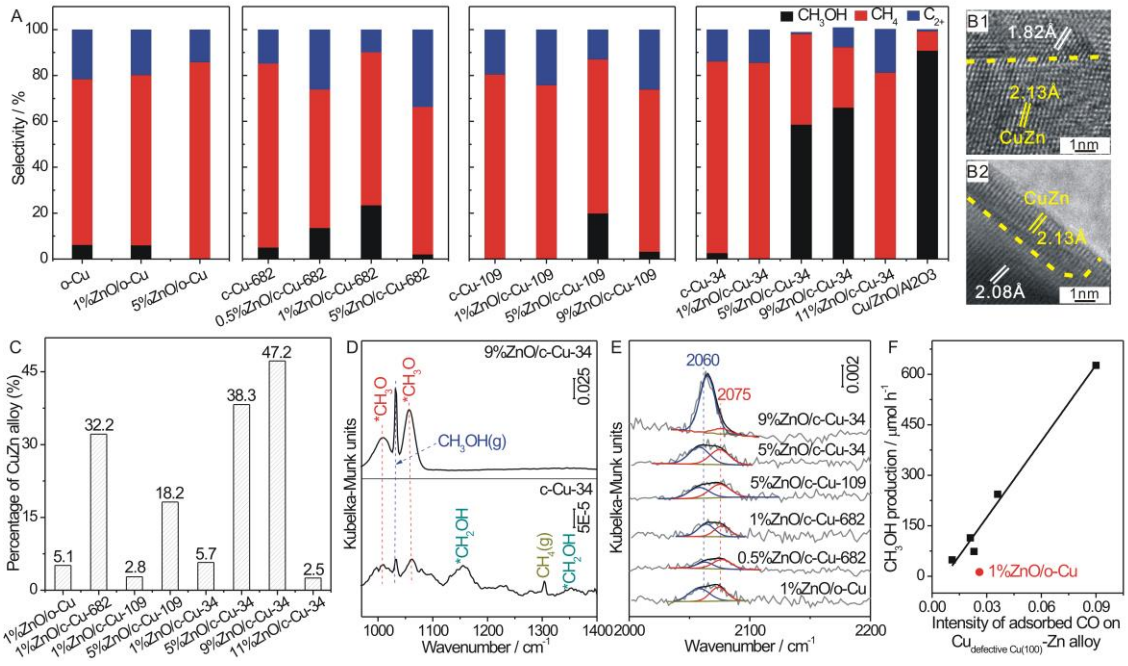

559

560 **Figure 4**. **Activity evaluations and mechanism investigations in CO hydrogenation**
561 **reaction. (A1-A4)** Catalytic performance of various Cu and ZnO/Cu catalysts in the CO
562 hydrogenation to methanol reaction; Representative HRTEM images of used (**B1**)
563 1%ZnO/c-Cu-682 and (**B2**) 1%ZnO/o-Cu; Lattice fringes of 1.82, 2.08, and 2.13 Å
564 respectively correspond to the spacing of Cu{100}. Cu{111} (JCPDS card NO. 89-2838),
565 and Zn-Cu alloy {111} (JCPDS card NO 89-1397) crystal planes; (**C**) Statistical
566 percentage of CuZn alloy nanoparticles of various ZnO/Cu catalysts derived from
567 corresponding HRTEM images; (**D**) In situ DRIFTS spectra of c-Cu-34 and 9%ZnO/c-
568 Cu-34 catalysts under 2 MPa 33.3% CO + 66.7% H_2 at 523 K; (**E**) In situ FT-IR spectra
569 with peak-fitting results of CO adsorbed on various ZnO/Cu catalysts evaluated after CO
570 hydrogenation to methanol reaction and (**F**) CH_3OH productions over various ZnO/Cu
571 catalysts as a function of the intensity of CO adsorbed on $Cu_{defective\ Cu(100)}$-Zn alloy
572 derived from corresponding DRIFTS results.

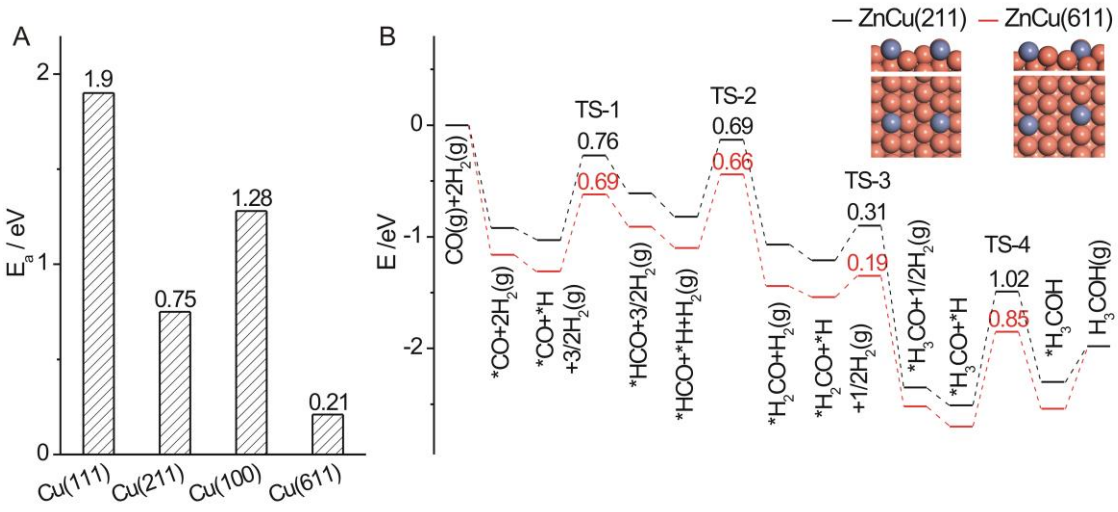

573

574 **Figure 5. DFT calculations in CO hydrogenation reaction. (A)** Calculated activation
575 energy for CuZn alloy formation of ZnO on various Cu surfaces and **(B)** Calculated
576 energy profiles of CO hydrogenation into methanol by ZnCu(211) and ZnCu(611) alloys.
577 Insets show the optimized surface structures of ZnCu(211) and ZnCu(611) alloys. The
578 reddish-orange and purple spheres represent Cu and Zn atoms, respectively.

Figures

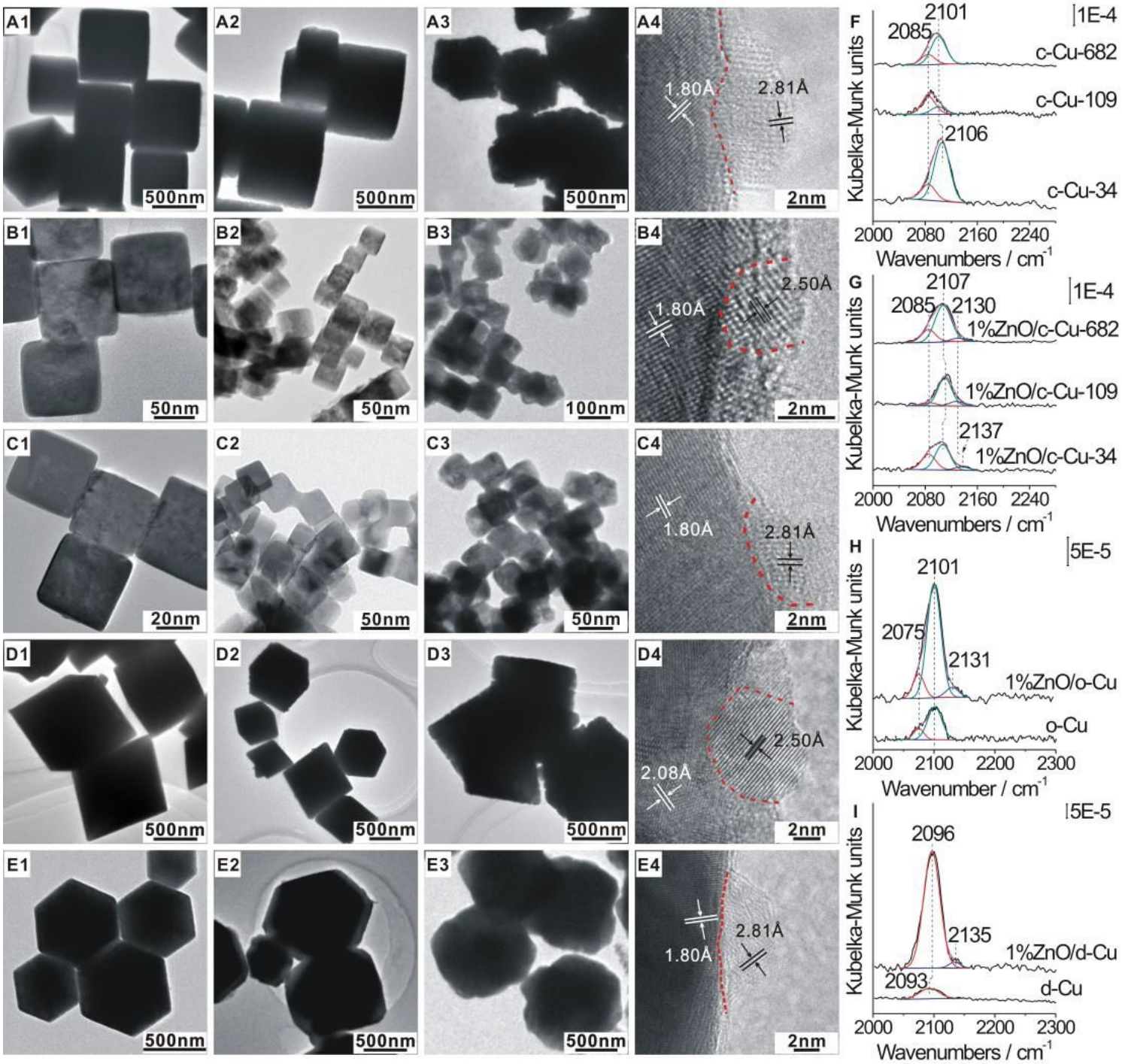

Figure 1

Structural characterizations. TEM images of as-synthesized (A1) c-Cu2O-524 682, (B1) c-Cu2O-109, (C1) c-Cu2O-34, (D1) o-Cu2O, and (E1) d-Cu2O NCs; TEM images of as-synthesized (A2) 1%ZnO/c-Cu2O-682, (B2) 1%ZnO/c-Cu2O-109, (C2) 1%ZnO/c-Cu2O-34, (D2) 1%ZnO/o-Cu2O, and (E2) 1%ZnO/d-Cu2O catalysts; TEM and HRTEM images of as-synthesized (A2) 1%ZnO/c-Cu-682, (B2) 1%ZnO/c-Cu-109, (C2) 1%ZnO/c-Cu-34, (D2) 1%ZnO/o-Cu, and (E2) 1%ZnO/d-Cu catalysts; In situ DRIFTS with peak-fitting

results of CO adsorption at 123 K on (F) various c-Cu NCs, (G) various 530 1%ZnO/c-Cu catalysts, (H) o-Cu NCs and 1%ZnO/o-Cu catalyst, and (I) d-Cu NCs and 1%ZnO/d-Cu catalyst. Lattice fringes of 1.80, 2.08, 2.50/2.51, 2.61, and 2.81 Å respectively correspond to the spacing of Cu{200}, Cu{111} (JCPDS card NO. 89-2838), 533 hexagonal ZnO{101}, ZnO{002}, and ZnO{100} (JCPDS card NO 89-1397) crystal 534 planes.

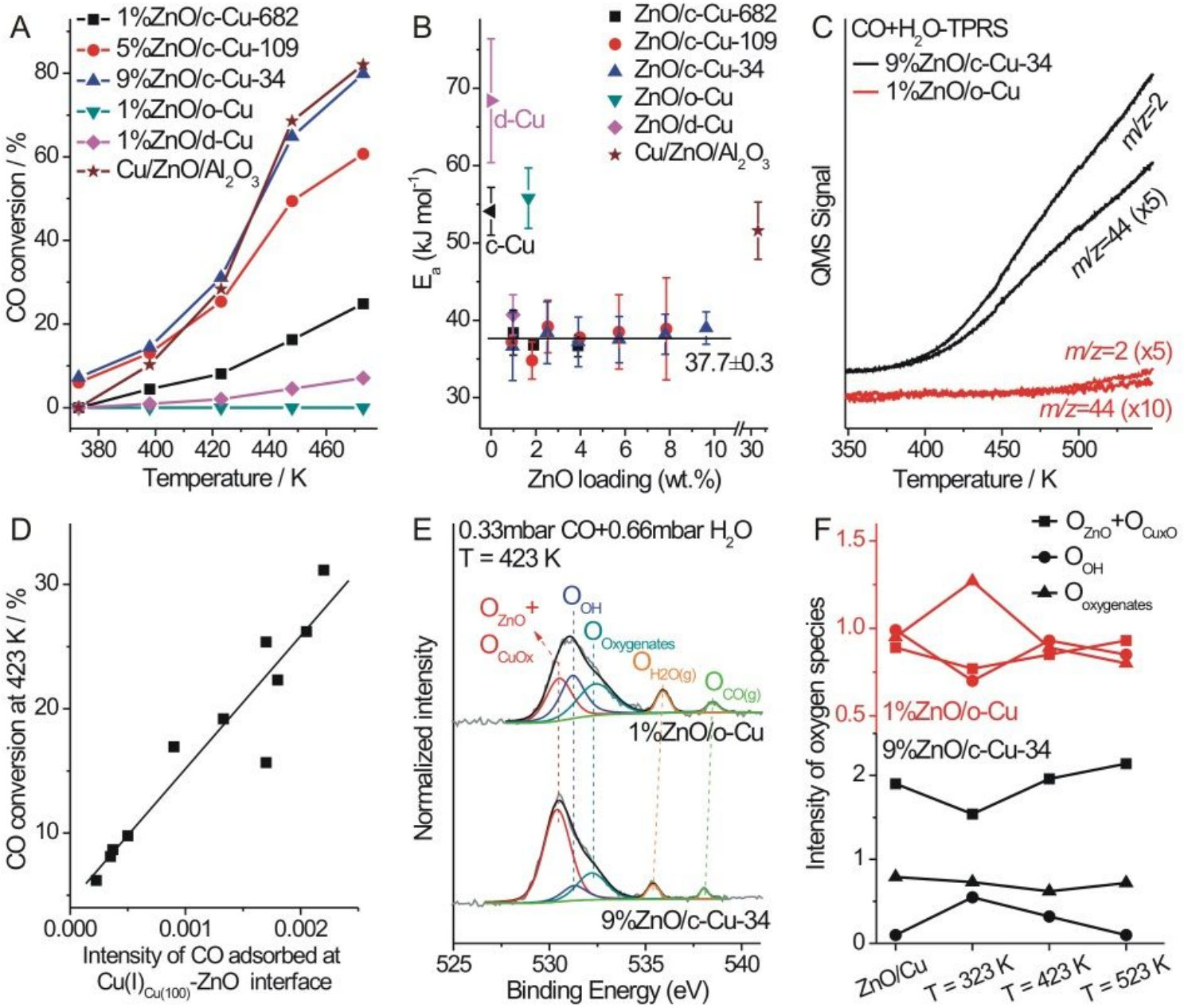

Figure 2

Activity evaluations and mechanism investigations in WGS reaction. (A) Catalytic performance of representative ZnO/Cu and commercial Cu/ZnO/Al2O3 WGS catalysts for the WGS reaction; (B) Apparent activation energies (Ea) of various Cu- based catalysts as a function of ZnO loadings; (C) Temperature-programmed reaction spectra of WGS reaction over 9%ZnO/c-Cu-34 and 1%ZnO/o-Cu catalysts; (D) CO conversion at 423 K as a function of the intensity of CO adsorbed on Cu(I)Cu(100)-ZnO interface derived

from corresponding DRIFTS results; (E) NAP-XPS spectra with peak-fitting results of 9%ZnO/c-Cu-34 and 1%ZnO/o-Cu catalysts under 0.33 mbar CO + 0.66 mbar H2O at 423 K; (F) Variations of the intensity of oxygen-containing species on 9%ZnO/c-Cu-34 and 1%ZnO/o-Cu catalysts under 0.33 mbar CO + 0.66 mbar H2O at different temperatures derived from corresponding NAP-XPS results.

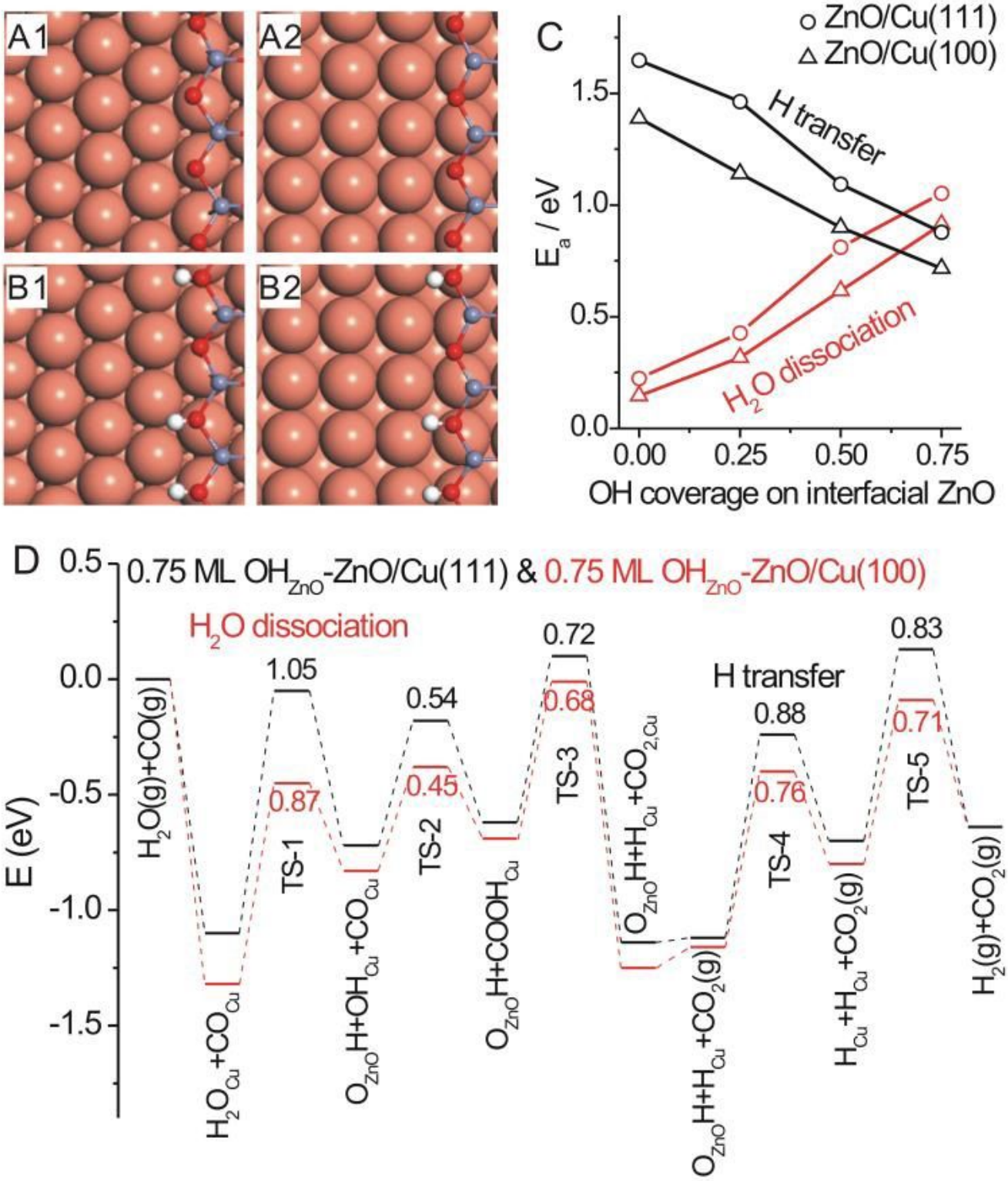

Figure 3

DFT calculations in WGS reaction. Optimized surface structures of (A1) ZnO/Cu(111), (A2) ZnO/Cu(100), (B1) 0.75 ML-OHZnO-ZnO/Cu(111) and (B2) 0.75 ML OHZnO-ZnO/Cu(100). The reddish-orange, purple, red, and white spheres represent Cu, Zn, O, and H atoms, respectively.; (C) Calculated activation energy of H2O dissociation and OHZnO-to-HCu H transfer reaction at ZnO-Cu interface as a function of the OH coverage on interfacial ZnO of ZnO/Cu(111) and ZnO/Cu(100) surfaces; (D) Calculated energy profiles of WGS reaction catalyzed by 0.75 ML OHZnO-ZnO/Cu(111) and 0.75 ML OHZnO-ZnO/Cu(100) surfaces.

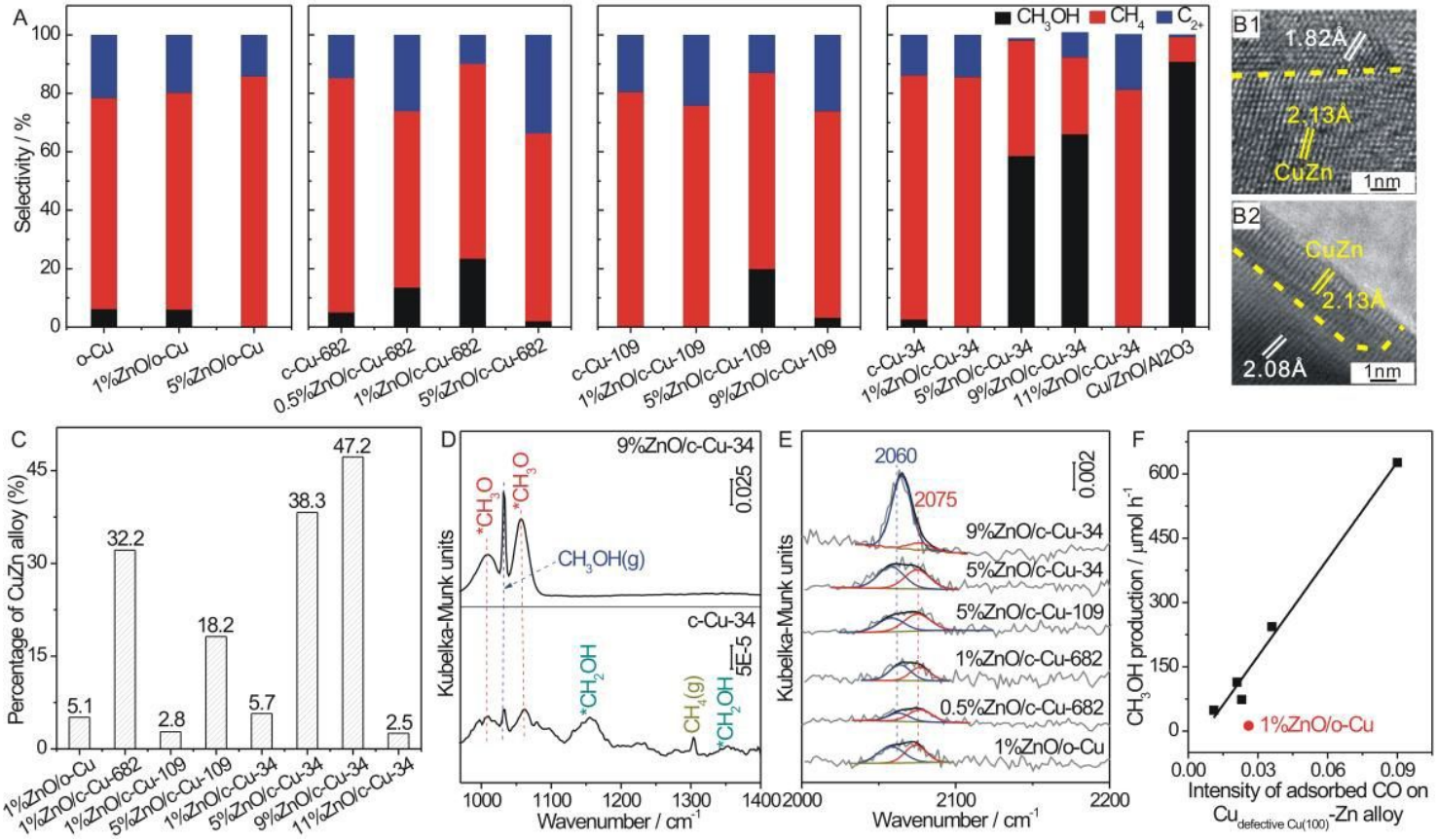

Figure 4

Activity evaluations and mechanism investigations in CO hydrogenation reaction. (A1-A4) Catalytic performance of various Cu and ZnO/Cu catalysts in the CO hydrogenation to methanol reaction; Representative HRTEM images of used (B1) 1%ZnO/c-Cu-682 and (B2) 1%ZnO/o-Cu; Lattice fringes of 1.82, 2.08, and 2.13 Å respectively correspond to the spacing of Cu{100}. Cu{111} (JCPDS card NO. 89-2838), and Zn-Cu alloy {111} (JCPDS card NO 89-1397) crystal planes; (C) Statistical percentage of CuZn alloy nanoparticles of various ZnO/Cu catalysts derived from corresponding HRTEM images; (D) In situ DRIFTS spectra of c-Cu-34 and 9%ZnO/c-Cu-34 catalysts under 2 MPa 33.3% CO + 66.7% H2 at 523 K; (E) In situ FT-IR spectra with peak-fitting results of CO adsorbed on various ZnO/Cu catalysts evaluated after CO hydrogenation to methanol reaction and (F) CH3OH productions over various ZnO/Cu catalysts as a function of the intensity of CO adsorbed on Cudefective Cu(100)-Zn alloy derived from corresponding DRIFTS results.

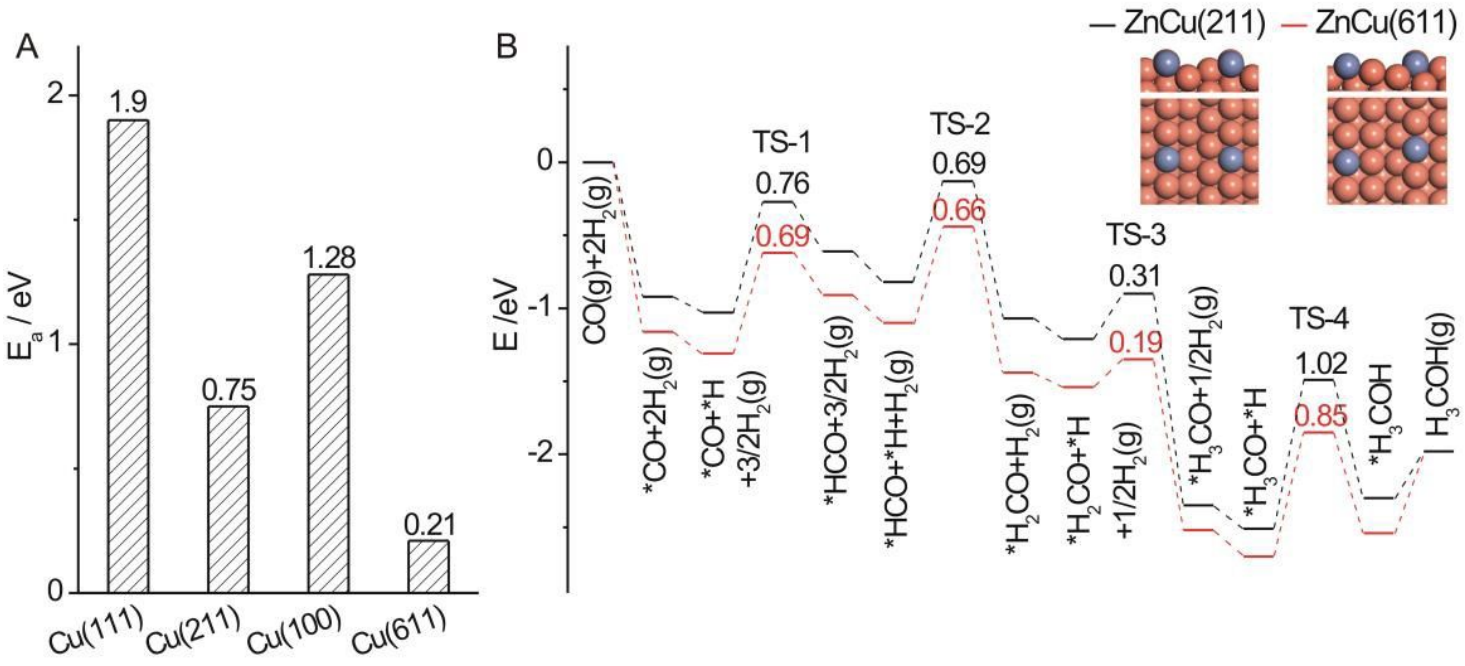

Figure 5

DFT calculations in CO hydrogenation reaction. (A) Calculated activation energy for CuZn alloy formation of ZnO on various Cu surfaces and (B) Calculated energy profiles of CO hydrogenation into methanol by ZnCu(211) and ZnCu(611) alloys. Insets show the optimized surface structures of ZnCu(211) and ZnCu(611) alloys. The reddish-orange and purple spheres represent Cu and Zn atoms, respectively.

Supplementary Files

This is a list of supplementary files associated with this preprint. Click to download.

- CuZnOMsSI.pdf